Improved Sensorless Control of Multiphase Synchronous Reluctance Machine Under Position Sensor Fault

Giuseppe Galati , *Student Member, IEEE*, Ludovico Ortombina , *Member, IEEE*, Luigi Alberti , *Senior Member, IEEE*, and Matteo Berto, *Student Member, IEEE*

Abstract—This article presents an investigation on the self-sensing capability of a dual three-phase synchronous reluctance motor. Self-sensing capability refers to the ability of the motor to properly operate in a sensorless drive. The multiphase machine is decomposed into two different three-phase systems according to the multistator approach. Several supply scenarios are studied where the two three-phase windings are controlled at different operating points along a reference trajectory. The analysis is carried out both with finite element analysis (FEA) simulations and experimental tests. In the first part of this article, the rotor is locked to derive the observer trajectories and find the regions in which the motor can operate without position sensor. A comparison between simulated and experimental results is given. Finally, a sensorless control strategy that allows exploiting the motor self-sensing capability under position sensor fault is developed and validated through etests.

Index Terms—Dual three-phase (DT) machine, fault tolerant, high-frequency injection, position observer, self-sensing capability, sensorless control, synchronous reluctance motor.

I. INTRODUCTION

IN THE last years, three-phase synchronous reluctance motors [1], [2] have seen increasing interest thanks to the absence of permanent magnets, no rotor losses, easy manufacturing, and their relatively low cost compared with the other types of permanent magnets synchronous motors (PMSMs) [3], [4]. Moreover, due to the enhanced attention on the fault-tolerant capability [5], [6], redundancy [7], and high power density, multiphase motors have attracted great attention. One of the main multiphase topology for a six-phase motor is a dual three-phase (DT) machine with two identical three-phase windings as it exhibits high reliability and employs commercial standard three-phase inverters.

An effective motor control relies on an accurate knowledge of the rotor position to achieve high performance. The position is obtained by means of an encoder or resolver, which increase the overall price and decrease the reliability of the system, indeed one of main common fault in a sensored drive is a fault in the position sensor. To remove the mechanical sensor, several estimation algorithms have been developed. These methods allow the removal of the position sensor by reducing the motor frame size, lowering the price, and increasing the reliability of the drive. According to the operating speed of the motor, these techniques can be bundled into two groups. In medium–high speed range, position observers based on fundamental frequency signals are implemented, such as those based on the back electromotive force or the active flux [8]. At standstill and low-speed region, additional high-frequency (HF) signal injected on the fundamental components [9] or unconventional pulsewidth modulation (PWM) patterns are exploited in order to depict the rotor anisotropy [10] and retrieve the rotor position. However, low-speed signal-injection sensorless controls are affected by an estimation error due to the motor cross-differential inductances. Stability issues and the estimator convergence could be affected due to the estimation error.

Low-speed sensorless algorithms and compensation techniques have been applied to multiphase machine in [11], [12], [13], [14], and [15]. In [12], a method taking advantage of the additional degree of freedom of DT motor is proposed, and it allowed for reducing both the torque and the dc-link current ripple. The method was applied to PMSM and a constant steady-state error is shown. A different approach is used in [13] where the HF signals are injected in only one three-phase electrical winding. The method is applied on a low-voltage PMSM and good performance is achieved. The zero-sequence voltage is exploited in [14] to estimate the rotor position and the undesired harmonic was suppressed by applying an optimal phase shift between the two independent injected signals. However, a quite large constant estimation error is reported. A compensation method based on current pulse injection is investigated in [15]. The additional degree of freedom of a PM DT motor is exploited to estimate motor parameters and, in turn, improve the sensorless accuracy.

Giuseppe Galati, Ludovico Ortombina, and Luigi Alberti are with the Department of Industrial Engineering, University of Padova, 35122 Padova, Italy (e-mail: giuseppe.galati@phd.unipd.it; ludovico.ortombina@unipd.it; luigi.alberti@unipd.it).

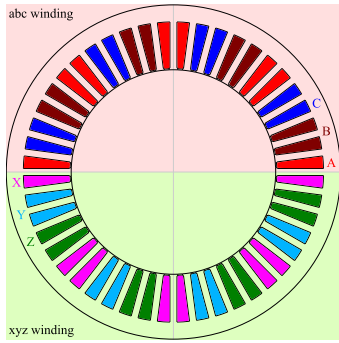Matteo Berto is with the BorgWarner Systems Engineering GmbH, 67292 Nuremberg, Germany (e-mail: Matteo.berto@phd.unipd.it).

Fig. 1. Adopted layout of the stator windings. One three-phase system is distributed at the top of the stator, the latter one at the bottom.

TABLE I
GEOMETRIC MOTOR DATA

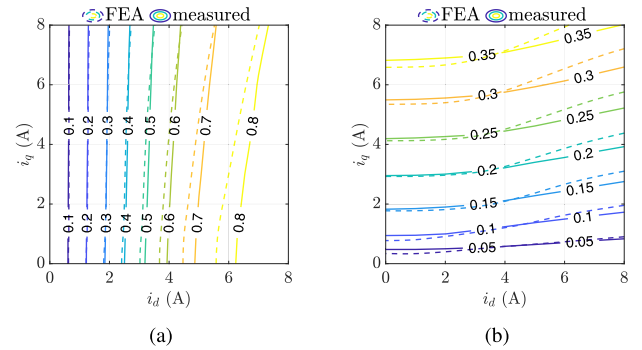| Parameter	Symbol	Value
Stack length	L_{stk}	85 mm
Number of slots	Q	46
series conductor per slot	n_c	46
parallel conductor per slot	n_p	1
Slot fill factor	k_{fill}	0.4
Air gap	g	0.4
Outer diameter	D_e	170 mm
Inner diameter	D_i	104 mm
Tooth width	w_t	3.6 mm
Slot height	h_s	24.3 mm
Number of barriers	n_b	3

Fig. 2. Flux linkage maps comparison between measured and FEA simulations in three-phase configuration. (a) $\lambda_d(i_d, i_q)$. (b) $\lambda_q(i_d, i_q)$.

This article proposes a low-speed sensorless control strategy based on the DT motor self-sensing capability. The self-sensing capabilities are evaluated for different operating conditions, as the three-phase configuration, the half-control (HC) one, and six-phase one, and an in-depth discussion is reported. In the case of mechanical sensor fault, a three-phase winding is controlled at low current and HF signals are injected to retrieve the rotor position. The reduced magnetic saturation due to the working condition allows for achieving an accurate rotor position estimation, which is used by both windings of the DT machine. The second three-phase winding can work until its nominal current and overloaded. The proposed control algorithm reduces the motor performance but it allows operation in the case of a mechanical sensor fault. Moreover, the estimated position is accurate and not affected by the estimation error due to cross-magnetic saturation that is the main flaw of low-speed algorithm and no motor parameters are required.

In [16], an experimental investigation of the self-sensing capability is carried out. In this article, finite element analysis (FEA) is included to study and compare experimental and simulated results. Flux linkage maps and theoretical observer trajectories for different supply scenarios are included. In addition, an improved experimental study is proposed with the online calculation of the estimation error and the observer trajectories for the three-phase configuration of the considered motor.

The rest of this article is organized as follows. The description and the analysis of the adopted motor are described in Section II. The sensorless drive and the proposed control technique are thoroughly described in Section III. The results are reported in Section IV. Finally, Section V concludes this article.

II. MOTOR DESCRIPTION AND MODELING

A DT synchronous reluctance machine is adopted in this article. The winding arrangement is shown in Fig. 1. It is composed by two identical three-phase windings labeled as abc and xyz where each electrical system is supplied by a dedicated inverter. The former one is distributed at the top of the stator, whereas the latter one at the bottom. The layout employed reduces the mutual inductances between the two windings, improving the fault-tolerant capability [17], [18], as one winding can be supplied, namely, HC mode, even if the other one is short-circuited. Table I

gives the main data of the motor. Further details of the motor design, the thermal analysis under fault operating conditions and its flux weakening capabilities can be found in [19] and [20].

In the following, both FEA analysis and experimental tests on the same motor to verify the accuracy of the proposed control strategy are reported. Flux linkage and torque maps have been measured and compared with FEA simulations for different supply configurations. Magnetic maps have been measured with a constant speed method and both windings have been fed with the current vector imposed in the dq plane. In Section II-A the three-phase configuration is analyzed, whereas in Section II-B, the HC mode is studied.

A. Three-Phase Configuration Analysis

In three-phase configuration, both windings are connected in series and supplied with the same current. Flux linkage maps are obtained both through FEA simulations and experimental measurements. The results are depicted in Fig. 2 and the flux density plot is shown in Fig. 5(a). Simulated results are akin to the measured one along both d- and q-axes in the rotating reference frame. A slight difference occurs when the motor is heavily saturated.

By means of the flux linkage maps, the simulated torque of the motor is calculated. Fig. 3 shows the comparison between simulated and measured torques.
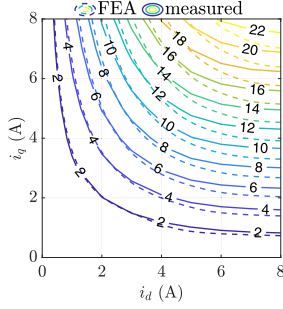
Fig. 3.   Torque map comparison between FEA and experimental measurements when the motor operates as three-phase system.
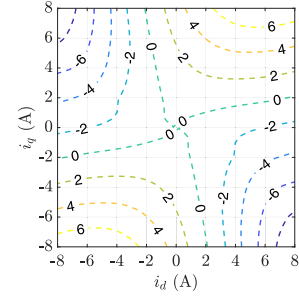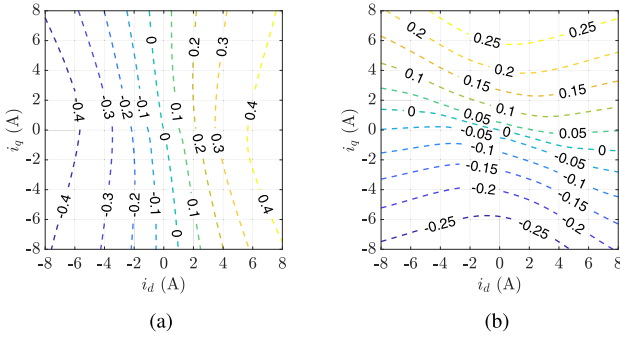

Fig. 4.   Flux linkages maps obtained through FEA simulations in half-condition mode (only the abc three-phase system is supplied). (a) $\lambda_d^{abc}(i_d, i_q)$. (b) $\lambda_q^{abc}(i_d, i_q)$.
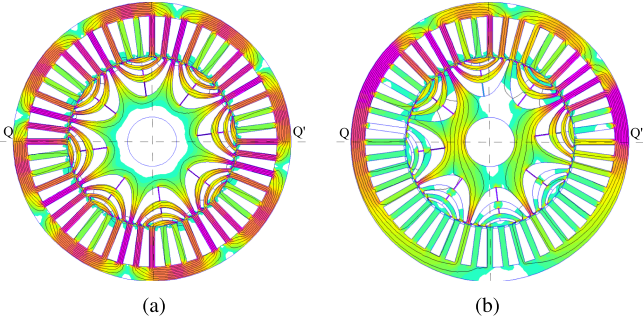

Fig. 5.   Flux density plot comparison. (a) Three-phase configuration. (b) HC configuration.

B. FEA Analysis in HC Condition

Only the abc winding is supplied during HC-mode. The motor is controlled as a single three-phase system and supplied by only one inverter. The xyz winding is completely open, hence no voltages and currents are applied to it. This is a particular scenario in which the motor can operate, for instance during a fault in the second three-phase winding. Fig. 4 shows the flux linkage maps $\lambda_d^{abc}(i_d, i_q)$ and $\lambda_q^{abc}(i_d, i_q)$ calculated through FEA simulations. The superscript on a variable means that the quantity refers to the indicated three-phase system. Same results can be obtained by supplying only the xyz winding.

The maps show that the magnetization of the motor is not homogeneous and symmetric. Flux density plot for the HC-mode

Fig. 6.   Torque map with FEA analysis during HC configuration.

when the mechanical rotor position $\vartheta_m = 0$ rad is depicted in Fig. 5(b). Flux lines flow in the stator area of the open xyz three-phase system, reducing the flux linkage in the supplied three-phase winding.

The torque map during the HC-condition is depicted in Fig. 6. The zero-value torque level is rotated with respect to the dq-current plane axes since the magnetic flux produced by the supplied three-phase winding is not bounded in the active region. In HC condition, the d- and q-axes flux linkage are not null even if the d-axis or the q-axis currents are zero, respectively, namely, $\lambda_d(0, i_q) \neq 0$ and $\lambda_q(i_d, 0) \neq 0$. It is worth reminding that the chosen winding configuration minimizes the mutual coupling between the two electrical systems and, in turn, the induced current in the case of a short-circuit in one of three-phase system [18], but exhibits a nonconventional torque map in the case of an open circuit fault.

III. SENSORLESS CONTROL

Sensorless algorithms estimate the rotor position by injecting HF signals on the fundamental one. Rotating injection is a position estimation method used at low speed, where two sinusoidal HF voltage signals are injected in the stationary reference frame

$$u_{h\alpha} = U_h \cos(\omega_h t) \qquad u_{h\beta} = U_h \sin(\omega_h t) \qquad (1)$$

and U_h and ω_h are magnitude and pulsation frequency of the injected sinusoidal waves. The injected HF voltage signals induce HF currents, which draw an ellipse in the $\alpha\beta$ reference frame. Its tilt contains the information related to the electrical rotor position ϑ_{me} obtained by multiplying the mechanical one ϑ_m for the pole pairs p. The elliptical trajectory due to the induced currents is centered on the fundamental current vector and can be fitted by using the implicit equation of a generic ellipse

$$a i_\alpha^2 + b i_\alpha i_\beta + c i_\beta^2 + d i_\alpha + e i_\beta = f \qquad (2)$$

which describes the measured stator currents in the stationary reference frame i_α and i_β. The ellipse fitting (EF) algorithm processes the measured currents by fitting current samples on the mathematical ellipse equation by exploiting the least square algorithm and avoiding any filters [21]. The estimated rotor position $\widetilde{\vartheta}_{me}$ can be retrieved from its sine and cosine components by means of a quadrature Q-PLL. The EF algorithm together with the Q-PLL forms the position estimator (PE). It is worth remembering that the selected estimation algorithm requires no
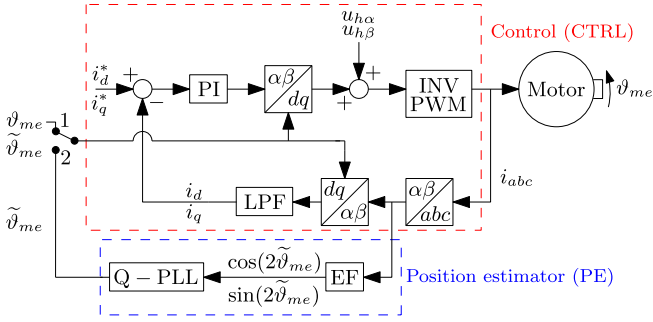
Fig. 7.   Control (CTRL) loop and PE scheme with rotating injection in $\alpha\beta$ and EF technique. The scheme is implemented for both windings. System operates in sensored mode when the switch is in position 1; otherwise, it operates in sensorless mode.

TABLE II
PLATE DATA OF THE MUT

Parameter	Symbol	Value
Rated voltage	V_n	350 V
Rated r/min	n_n	1000 r/min
Pole pairs	p	4
Nominal current	I_n	8.3 A
Nominal torque	T_n	14 N m

TABLE III
SENSORLESS DRIVE PARAMETERS

Parameter	Symbol	Value
Injection magnitude	U_h	100 V
Injection frequency	f_h	1000 Hz

motor parameters knowledge for the position estimation, so it is inherently robust against parameter mismatches.

To close the current control loop, the HF currents in the rotating reference frame are filtered by means of a low-pass filter (LPF). The filtered currents i_d and i_q are then used as feedback and compared with the reference one i_d^* and i_q^*. Proportional–integrator (PI) controllers are designed to drive the error to zero and calculate the fundamental reference voltages. Fig. 7 shows the adopted scheme for the motor control and position estimation for a single three-phase system. The aforementioned blocks together with the HF injection and the inverter pulse width modulation constitute the control (CTRL) loop of the motor.

A. Self-Sensing Capability

Self-sensing capability refers to the ability of a motor to be properly controlled in low-speed sensorless mode. Magnetic saturation and cross-coupling negatively affect estimator's performance. The former reduces the detectable anisotropy, whereas the latter one induces a position estimation error, which degrades the electric drive performance and it could lead to stability issues. The estimated rotor position $\widetilde{\vartheta}_{me}(i_d, i_q)$ differs from the actual one by the estimation error as

$$\widetilde{\vartheta}_{me}(i_d, i_q) = \vartheta_{me} + \epsilon(i_d, i_q) \tag{3}$$

where ϑ_{me} is the actual electromechanical rotor position and $\epsilon(i_d, i_q)$ is the estimation error. It can be computed as

$$\epsilon(i_d, i_q) = 0.5 \operatorname{atan2}(l_{dq}(i_d, i_q), -l_\Delta(i_d, i_q)) \tag{4}$$

where $l_{dq}(i_d, i_q)$ is the cross-differential inductance obtained as $\partial\lambda_d(i_d, i_q)/\partial i_q = \partial\lambda_q(i_d, i_q)/\partial i_d$ and l_Δ is the semidifference inductance defined as the difference between the self-differential inductances $l_\Delta(i_d, i_q) = (l_{dd}(i_d, i_q) - l_{qq}(i_d, i_q))/2$. It is worth noting that the estimation error ϵ depends on the operating point since saturation and cross-saturation inductance vary according to the current operating point. At low current cross-saturation inductance is usually negligible and, in turn, the estimation error. As the current increases ϵ becomes more relevant.

In a sensored electric drive, the current control loops work in the actual dq reference frame and the operating point coincides with the reference (REF) one. The estimator works in open-loop mode indeed the estimated position $\widetilde{\vartheta}_{me}$ does not affect the control. The estimation error ϵ can be computed for any current level along a predetermined reference trajectory. It can be depicted in the dq current plane by

$$i_d^x = i_d \cos(\epsilon(i_d, i_q)) - i_q \sin(\epsilon(i_d, i_q))$$
$$i_q^x = i_d \sin(\epsilon(i_d, i_q)) + i_q \cos(\epsilon(i_d, i_q)) \tag{5}$$

where i_d^x and i_q^x represent the current operating point rotated by the estimation error, so the trajectory t_1 is obtained. The trajectory t_1 exists for any current level, since the drive is not affected by the observer and, in turn, by its estimation error. Finally, it is worth noting that the electric drive does not work along the sensored trajectory t_1 since it is only a graphical expedient to show the observer's estimation error for any load level.

In a sensorless electric drive, the estimated position is used to perform the Park transformation and to compute the speed feedback, so the estimator performance and its accuracy affect the overall electric drive behavior. The motor operates along the trajectory t_2, which differs from t_1, and an effective method to compute it is derived in [22]. The trajectory t_2 represents the electric drive operating locus in sensorless mode computed from a reference trajectory. The trajectory t_2 does not exist for any current level, since if the estimation error is too large, no stable points exist for the overall system, leading the electric drive in unstable condition. Stable points around t_2 can be found by computing the intersection between the condition where the HF currents are zero and their derivate with respect the current angle has negative slope [23].

IV. RESULTS

The proposed sensorless control strategy and the self-sensing capability of the motor under test (MUT) are verified throughout an extensive experimental stage. The MUT is a DT synchronous reluctance motor, whose parameters are given in Table II. The injection quantities are listed in Table III. The sampling frequency is equal to the switching one at 10 kHz. The test bench is shown in Fig. 8. The MUT is coupled to a 4.5-kW PMSM, which is supplied by its own inverter. The PMSM, namely, master
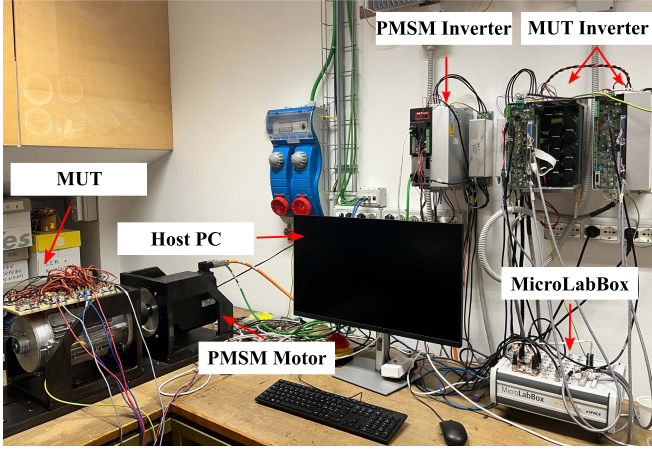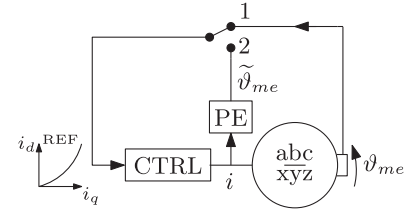
Fig. 8. Test bench experimental setup.

Fig. 9. Block scheme of the experiment during the three-phase configuration. When the switch is closed on position 1, the motor operates in sensored mode; otherwise, it operates sensorless. The MUT follows a rampwise reference.
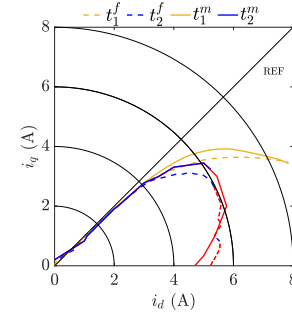

Fig. 10. Observer trajectories comparison between measured (t_1^m, t_2^m) and simulated (t_1^f, t_2^f) ones when the motor operates as a three-phase system. Unstable points around the trajectory t_2 are highlighted in red line.

motor, enables to drag the MUT at a fixed speed. The MUT is controlled along a reference trajectory and each three-phase winding is supplied by its own inverter. The control algorithm is implemented on a dSpace MicroLabBox platform connected to the host PC. Current controllers are designed to achieve a bandwidth of 100 Hz.

Five different tests are carried out to study the self-sensing capabilities of the motor and to verify the effectiveness of the proposed method. The first test is aimed to study the self-sensing capability of the motor when the two three-phase windings are connected in series. In this scenario the motor is supplied by only one inverter, namely, in three-phase configuration. This test is reported in Section IV-A. The second test investigates the HC-mode, hence only the one winding is supplied and the other one disconnected. This scenario is reported in Section IV-B. The interaction between the two three-phase systems and its effect on the self-sensing capability is investigated in Section IV-C by controlling the two three-phase windings in different operating points. The condition where both three-phase windings are supplied with different control strategies by two separate inverter is hereafter called six-phase control. In Section IV-D, the control loops of both windings are closed on the estimated position obtained from the electrical system operating at low current along REF. These tests are implemented at locked rotor $\vartheta_m = 0$ rad, namely, at standstill condition. In Section IV-E, the MUT is coupled to a PMSM and dragged at 50 r/min to test the effectiveness of the control strategy developed in Section IV-D at low speed.

A. Three-Phase Configuration

Both three-phase windings are connected in series to operate the motor in three-phase configuration. The result is a single three-phase machine; therefore, a unique estimator is used to retrieve the rotor position. The layout of the experiment is shown in Fig. 9. When the switch is in position 1, the current control operates with the actual measured position and the estimated one is exploited to compute the sensored trajectory t_1. With the switch in position 2, the CTRL is closed on the estimated

position and the electric drive operates in the estimated rotating reference frame, so the sensorless trajectory t_2 can be obtained.

Fig. 10 shows the comparison between the trajectories measured during the experimental test (t_1^m, t_2^m) and computed by FEA magnetic maps (t_1^f, t_2^f). Experimental and simulated results look very similar. For current magnitude lower than 4 A, the estimation error is almost negligible being t_1 almost overlapped to the reference. The sensorless trajectory t_2 is overlapped as well, since estimation error does not affect the electric drive. For higher current values, an estimation error appears, and it affects the sensorless operation. The trajectory t_2 starts to diverge, according to the analysis carried out in Section III-A. For current values higher than 5.5 A, the system becomes unstable since the open loop estimation error is quite large (see t_1) and a convergence point does not exist for the observer. It is worth highlighting that not all the points around t_2 are stable. Indeed the points both in red line both for FEA and experimental measurement represents the unstable points around the sensorless trajectory as discussed in Section III-A.

B. Half Control

In HC-mode, only one three-phase system is supplied. A schematic of the experiment is shown in Fig. 11. The observer trajectories are calculated as in the previous test. The experimental trajectories are compared with the theoretical one obtained by the Apollo software. The comparison is shown in Fig. 12. The measured and the simulated observer trajectories are comparable. A slightly difference can be noted at low current where the simulated trajectories are overlapped but not with the
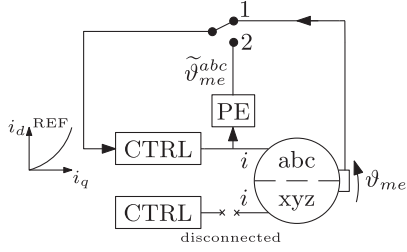
Fig. 11. Block scheme of the experiment during the HC-condition. The abc winding is supplied and the xyz one disconnected.
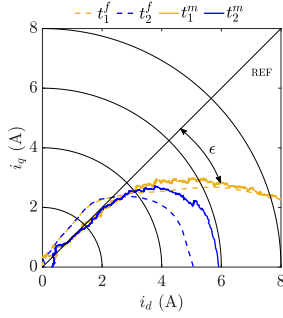

Fig. 12. Observer trajectories comparison between measured (t_1^m, t_2^m) and simulated (t_1^f, t_2^f) analysis when the motor operates in HC-mode.
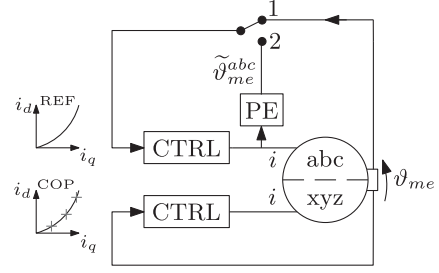

Fig. 13. Six-phase control: part 1 block scheme of the experiment. Estimation winding is supplied and operate at COP along REF. Its control loop is closed on the measured position during both the load winding observer trajectories calculation.
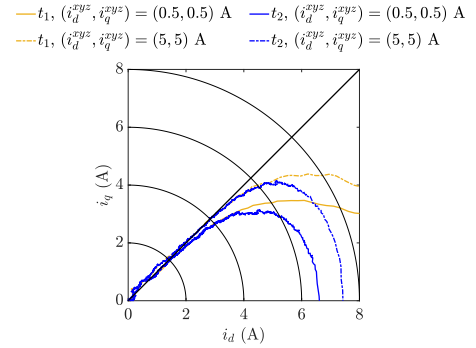

Fig. 14. Six-phase control: part 1. Load winding observer trajectories when the estimation winding operates at COP. Its control loop is closed on the measured position for both the load winding observer trajectories calculation.

reference and the measured one. The current value at which the trajectories are overlapped is the same both for experimental and simulated results and it is equal to 3 A. At higher current values, the sensored trajectories t_1^m and t_1^f are almost the same. The simulated sensorless trajectory t_2^f exhibits convergence issue for current values close to 4.5 A. While the measured sensorless trajectory t_2^m is slightly wider than the simulated one, showing that real operational limit for sensorless operation is slightly higher.

In the following tests, the xyz winding is controlled at constant operating point (COP), whereas the abc one follows a rampwise current reference, as in previous tests. In addition HF signals are injected in both windings to estimate the rotor position. The estimated rotor position with the abc winding is used to study the self-sensing capability of the motor and trace the trajectory t_1 and t_2, whereas the xyz estimated rotor position is exploited to compute the Park transformation in the closed-loop control. For this reason, the abc winding is called *load* one and the xyz one is referred as *estimation* winding.

C. Six-Phase Control: Part 1

This test investigates the effects of the operating point of the estimation winding on the self-sensing capability of the load one. t_1 and t_2 are calculated by implementing the PE in the load winding as in the previous tests but the estimation winding is supplied and it operated at COP. Moreover, the estimation winding control loop is closed on the measured position. A block scheme of the experiment is depicted in Fig. 13. The results of the experiments are shown in Fig. 14 where two

operating points are evaluated, namely, $(i_d, i_q) = (0.5, 0.5)$ A and $(5, 5)$ A. The self-sensing capability of the load winding is improved in the second case indeed both trajectories t_1 and t_2 follow the reference line for a larger segment and the sensorless trajectory becomes unstable at a higher current level. It is worth remembering that when the sensored and sensorless trajectories overlap with the reference, no estimation error is detected.

FEA analysis is carried out to investigate the obtained results. The open source package Dolomites [24] is used to calculate the estimation error of the load winding in the same scenario experimentally analyzed and results are shown in Fig. 15. A plateau can be recognized from 4 to 6 A when the estimation winding operates at 5 A. In this range, the estimation error of the load winding is lower than the 0.5 A load winding operating condition. It is worth noting that the plateau is located where the self-sensing capability of the machine increases in accordance with the experimental evidences.

D. Six-Phase Control: Part 2

In the test described in Section IV-C, a negligible estimation error is observed with the estimation winding partially loaded indeed both sensored and sensorless trajectories overlap the reference one. This test exploits previous results and verifies the self-sensing capability of the motor in complete sensorless operating mode. The measured rotor position is used only for checking the estimation accuracy. The estimation winding is
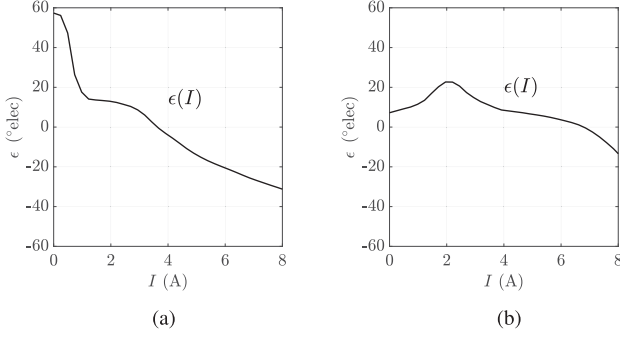
Fig. 15. Six-phase control: part 1. Open loop estimation error of the load winding. The estimation one is supplied at COP and its control loop closed on the measured position. (a) $(i_d^{xyz}, i_q^{xyz}) = (0.5, 0.5)$ A. (b) $(i_d^{xyz}, i_q^{xyz}) = (5, 5)$ A.
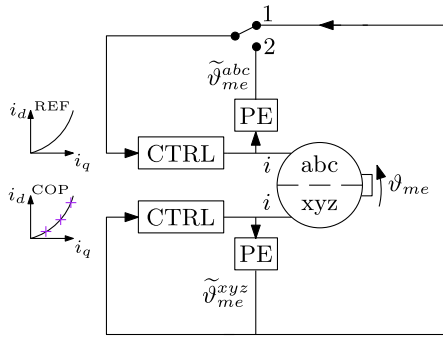

Fig. 16. Six-phase control: part 2 block scheme of the experiment. Estimation winding is supplied and operate at COP along REF. its estimated position $\widetilde{\vartheta}_{me}^{xyz}$ replaces the measured one. When the switch is in position 1, the motor operates in complete sensorless mode.
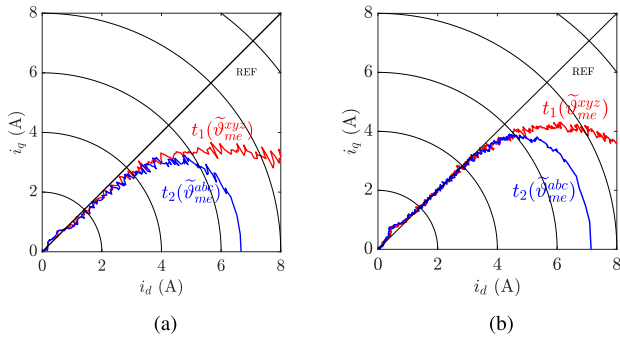

Fig. 17. Six-phase control: part 2. Load winding observer trajectories when $\widetilde{\vartheta}_{me}^{xyz}$ from the estimation winding replaces the measured one. (a) $(i_d^{xyz}, i_q^{xyz}) = (1, 1)$ A. (b) $(i_d^{xyz}, i_q^{xyz}) = (3, 3)$ A.

controlled to a low current COP as a negligible estimation error is obtained. The estimated rotor position $\widetilde{\vartheta}_{me}^{xyz}$ is used by the control of the estimation winding as well as the load one during the tracing of the trajectory t_1. The estimated position $\widetilde{\vartheta}_{me}^{abc}$ is used to measure the sensorless trajectory t_2, as in previous tests. Fig. 16 depicts the block scheme of the experiment.

Fig. 17 shows the experimental results obtained with the estimating three-phase system working in two different COP.
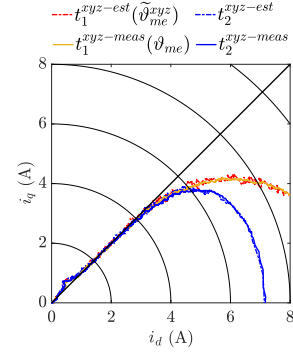

Fig. 18. Comparison of the load winding observer trajectories when the estimation one operates at 3 A in complete sensorless and sensored mode.
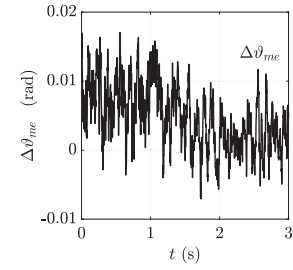

Fig. 19. Six-phase control: part 2. Estimation error between the measured position and the estimated one from the estimation winding $\widetilde{\vartheta}_{me}^{xyz}$ working at $(i_d^{xyz}, i_q^{xyz}) = (3, 3)$ A. Standstill operation in complete sensorless mode.

The sensorless trajectory t_2 is computed as follows:

$$i_d^x = i_d \cos(\widetilde{\vartheta}_{me}^{abc} - \widetilde{\vartheta}_{me}^{xyz}) - i_q \sin(\widetilde{\vartheta}_{me}^{abc} - \widetilde{\vartheta}_{me}^{xyz})$$
$$i_q^x = i_d \sin(\widetilde{\vartheta}_{me}^{abc} - \widetilde{\vartheta}_{me}^{xyz}) + i_q \cos(\widetilde{\vartheta}_{me}^{abc} - \widetilde{\vartheta}_{me}^{xyz}) \quad (6)$$

where the measured position is replaced by the estimated $\widetilde{\vartheta}_{me}^{xyz}$. It can be noted that the self-sensing capability of the load winding is superior when the estimation winding has a higher current, according to the analysis carried out in Section IV-C.

Fig. 18 compares both sensored and sensorless trajectories obtained by closing the xyz winding control with the measured position or the estimated one. Both trajectory perfectly overlaps, confirming the developed control strategy. Measured rotor position can be replaced without self-sensing capability degradation by the estimated one obtained with a three-phase electrical system operating at low current level.

It is worth remembering that the complete sensorless mode just analyzed refers to the condition where the rotor of the motor is locked. It is equivalent to the motor operating at zero or standstill condition. The estimation error between the measured position and $\widetilde{\vartheta}_{me}^{xyz}$ is shown in Fig. 19, and it is negligible as smaller than 0.02 rad. This is further proof of good performance of the proposed control strategy under zero or standstill conditions.
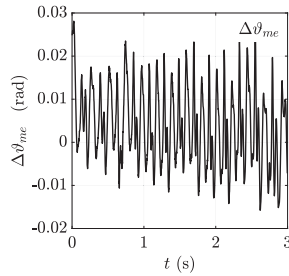
Fig. 20. Six-phase control: part 3. Estimation error between the measured position and $\widetilde{\vartheta}_{me}^{xyz}$ from the estimation winding working at $(i_d^{xyz}, i_q^{xyz}) = (3,3)$ A. Complete sensorless operation when the motor rotates at 50 r/min.
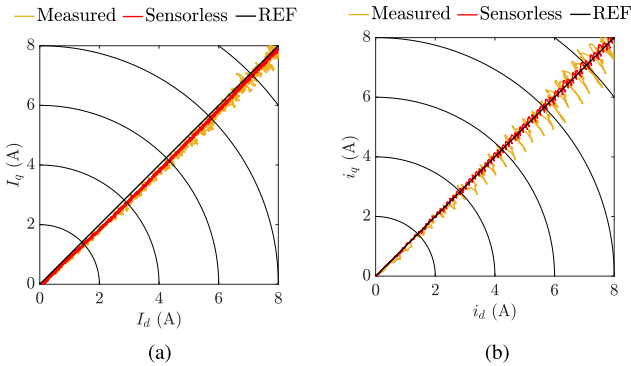

Fig. 21. Six-phase control part 3. Load winding current in the rotating reference frame obtained both with the measured and estimated rotor position. Both standstill and steady state at 50 r/min tests are reported. (a) Standstill condition. (b) Steady-state condition.

E. Six-Phase Control: Part 3

The aim of this section is further validate the proposed postfault sensorless control. The motor is coupled to a PMSM motor and dragged at 50 r/min. Both control loops are closed on the estimated position obtained by the estimating winding operating at low current, as in test carried out in Section IV-D. The load winding is controlled to follow a current reference till its nominal value. Fig. 20 depicts the position estimation error during the test, which amplitude is comparable with the one shown in Fig. 19. It is worth remembering that both tests are carried out in the same conditions, except for the operating motor speed. Fig. 21 depicts the current trajectory of the load winding in the rotating current plane obtained by using the measured or the estimated rotor position. The current reference line is depicted, as well. For sake of comparison, both standstill and steady-state condition tests are reported. The load winding exhibits a stable behavior since current follows the desired reference. It is worth noting that a 40% overload current is applied in both tests without any stability issue. In such a condition, the motor is expecting to produce almost 70% of the rated nominal torque from FEA simulation analysis. The estimating winding provided a reliable and error-free rotor position estimation since it works at low current values where the cross-coupling effect is negligible. In turn, the load winding is able to work in the desired working condition even in overload. Finally, it is worth noting that the sensorless trajectory t_2 diverged around 5 A in the HC test (see Section IV-B) where the load winding is closed on the estimated position obtained by its estimator (the xyz electrical system is disconnected), whereas the proposed scheme exhibits a stable behavior over the whole current range.

V. Conclusion

A postfault sensorless control strategy based on the study of the self-sensing capability of a DT synchronous reluctance motor is investigated in this article. Different supply scenarios, namely, three-phase and HC conditions, has been analyzed, and FEA analysis and experimental results are compared. In both configurations, the motor is not able to operate in sensorless mode at full load since the system is unstable due to the large estimation error induced by the cross-saturation inductance. The peculiar self-sensing capability and the additional degree of freedom of a DT motor are exploited by the proposed low-speed sensorless strategy. The former three-phase electrical winding operates at low speed and estimates the rotor position by injecting a HF rotating signal in the stator reference frame. The EF estimation algorithm is exploited to retrieve the rotor position since no motor parameters knowledge are required for its design and tuning. The negligible magnetic saturation at low-load condition allows an error-free rotor position estimation, which is used by both three-phase electric drives. The latter electric system can operate and accurately follow its current reference, even in overload condition. An extended experimental campaign proved the proposed control strategy. The proposed sensorless algorithm allows for controlling a dual-three synchronous reluctance motor in mechanical sensor postfault condition. No motor parameters are required for the estimation of the rotor position as well as compensation algorithm. The motor performance is reduced as a three-phase system that must work at low current level, but the service continuity is guaranteed and the motor is able to exploit up to 70% of the nominal torque in the analyzed condition.

References

[1] J. Kaska, T. Orosz, P. Karban, I. Dolezel, R. Pechanek, and D. Panek, "Optimization of reluctance motor with printed rotor," in *Proc. 22nd Int. Conf. Comput. Electromag. Fields*, 2019, pp. 1–4.

[2] S. P. Bosson, S. Janous, T. Kosan, and Z. Peroutka, "Real- time fault detection algorithm for interior permanent magnet synchronous motor drive using DSP/FPGA," in *Proc. IEEE 31st Int. Symp. Ind. Electron.*, 2022, pp. 655–660.

[3] A. Dianov, A. Anuchin, and A. Bodrov, "Robust MTPA control for steady-state operation of low-cost IPMSM drives," *IEEE J. Emerg. Sel. Topics Ind. Electr.*, vol. 3, no. 2, pp. 242–251, Apr. 2022.

[4] X. Zhang and Z. Liu, "Robustness optimization of model predictive current control for PMSM drives considering dynamic response influence," *IEEE J. Emerg. Sel. Topics Ind. Electr.*, vol. 4, no. 2, pp. 678–687, Apr. 2023.

[5] W. Wang, J. Zhang, M. Cheng, and S. Li, "Fault-tolerant control of dual three-phase permanent-magnet synchronous machine drives under open-phase faults," *IEEE Trans. Ind. Electron.*, vol. 32, no. 3, pp. 2052–2063, Mar. 2017.

[6] A. Mohammadpour, S. Mishra, and L. Parsa, "Fault-tolerant operation of multiphase permanent-magnet machines using iterative learning control," *IEEE Trans. Emerg. Sel. Topics Power Electron.*, vol. 2, no. 2, pp. 201–211, Jun. 2014.

[7] G. Rezazadeh, F. Tahami, G.-A. Capolino, Z. Nasiri-Gheidari, H. Henao, and M. Sahebazamani, "Improved design of a six-phase squirrel cage induction motor with pseudo-concentrated windings," *IEEE J. Emerg. Sel. Topics Ind. Electr.*, vol. 3, no. 4, pp. 1187–1194, Oct. 2022.

[8] I. Boldea and S. C. Agarlita, "The active flux concept for motion-sensorless unified ac drives: A review," in *Proc. Int. Aegean Conf. Elect. Mach. Power Electron. Electromotion Joint Conf.*, 2011, pp. 1–16.

[9] V. Manzolini and S. Bolognani, "On the rotor position self-sensing capability of reluctance and IPM synchronous motors," *IEEE Trans. Ind. Electron.*, vol. 56, no. 4, pp. 3755–3766, Jul./Aug. 2020.

[10] S. Bolognani, S. Calligaro, R. Petrella, and M. Sterpellone, "Sensorless control for IPMSM using PWM excitation: Analytical developments and implementation issues," in *Proc. Symp. Sensorless Control Electr. Drives*, 2011, pp. 64–73.

[11] H. Chen, Q. Gao, T. Yang, and M. Sumner, "Fundamental PWM excitation based rotor position estimation for a dual three-phase permanent magnet synchronous machine," *IEEE J. Emerg. Sel. Topics Ind. Electr.*, vol. 4, no. 2, pp. 659–668, Apr. 2023.

[12] M. Roetzer, U. Vollmer, L. Chen, and R. Kennel, "Anisotropy-based position estimation approach for symmetrical dual three-phase permanent magnet synchronous machines," in *Proc. IEEE Int. Symp. Sensorless Control Electr. Drives*, 2017, pp. 157–164.

[13] X. Bin, X. Luo, L. Zhu, and J. Zhao, "Sensorless control of dual three-phase PMSM with high frequency voltage signal injection," in *Proc. 22nd Int. Conf. Electr. Mach. Syst.*, 2019, pp. 1–4.

[14] A. H. Almarhoon, Z. Q. Zhu, and P. L. Xu, "Improved pulsating signal injection using zero-sequence carrier voltage for sensorless control of dual three-phase PMSM," *IEEE Trans. Energy Convers.*, vol. 32, no. 2, pp. 436–446, Jun. 2017.

[15] T. Liu, Z. Q. Zhu, Z.-Y. Wu, D. Stone, and M. Foster, "A simple sensorless position error correction method for dual three-phase permanent magnet synchronous machines," *IEEE Trans. Energy Convers.*, vol. 36, no. 2, pp. 895–906, Jun. 2021.

[16] G. Galati, L. Ortombina, L. Alberti, and M. Berto, "Investigation on the self-sensing capability of a dual three-phase synchronous reluctance machine," in *Proc. Int. Conf. Electr. Mach.*, 2022, pp. 2256–2262.

[17] J.-K. Park, C. Babetto, G. Berardi, J. Hur, and N. Bianchi, "Comparison of fault characteristics according to winding configurations for dual three-phase synchronous reluctance motor," *IEEE Trans. Ind. Electron.*, vol. 57, no. 3, pp. 2398–2406, May 2021.

[18] L. Ortombina, I. Husain, L. Alberti, and N. Bianchi, "Experimental evaluation of flux–weakening capability of dual three-phase synchronous reluctance motor," in *Proc. Int. Aegean Conf. Electr. Mach. Power Elec. Int. Conf. Opt. Electr. Elec. Equip.*, 2021, pp. 420–425.

[19] M. Popescu, D. G. Dorrell, L. Alberti, N. Bianchi, D. A. Staton, and D. Hawkins, "Thermal analysis of duplex three-phase induction motor under fault operating conditions," *IEEE Trans. Appl. Ind.*, vol. 49, no. 4, pp. 1523–1530, Jul. 2013.

[20] C. Babetto, N. Bianchi, A. Torreggiani, C. Bianchini, M. Davoli, and A. Bellini, "Design optimization and analysis of a synchronous reluctance machine for fault-tolerant applications," in *Proc. IEEE Int. Electr. Mach. Drv. Conf.*, 2019, pp. 1784–1791.

[21] L. Ortombina, M. Berto, and L. Alberti, "Sensorless drive for salient synchronous motors based on direct fitting of elliptical-shape high-frequency currents," *IEEE Trans. Ind. Electron.*, vol. 70, no. 4, pp. 3394–3403, Apr. 2023.

[22] M. Berto, L. Alberti, and S. Bolognani, "Experimental investigation on the self-sensing capability of synchronous machines for signal injection sensorless drives," in *Proc. IEEE Energy Convers. Congr. Expo.*, 2021, pp. 5078–5083.

[23] M. Berto, L. Alberti, V. Manzolini, and S. Bolognani, "Computation of self-sensing capabilities of synchronous machines for rotating high frequency voltage injection sensorless control," *IEEE Trans. Ind. Electron.*, vol. 69, no. 4, pp. 3324–3333, Apr. 2022.

[24] Dolomites, a package for the design of electric machines and drives. Accessed: May 2023. [Online]. Available: https://gitlab.com/LuigiAlberti/dolomites-python/-/tree/master/

Giuseppe Galati (Student Member, IEEE) received the B.S. and M.S. degrees in electrical engineering in 2018 and 2020, respectively, from the University of Padova, Padova, Italy, where he is currently working toward the Ph.D. degree in electrical engineering with the Electrical Drives Laboratory.

His main research interests include sensorless and embedded control of three-phase and multiphase ac motors.

Ludovico Ortombina (Member, IEEE) received the M.S and Ph.D. degree in mechatronics engineering from the University of Padova, Padova, Italy, in 2015 and 2019, respectively.

Since August 2020, he is a Researcher with the Department of Industrial Engineering, University of Padova. His research interests include parameter estimation techniques for synchronous motors, sensorless controls, and predictive control.

Luigi Alberti (Senior Member, IEEE) received the Laurea and the Ph.D. degrees in electrical engineering from the University of Padova, Padova, Italy, in 2005 and 2009, respectively.

From 2009 to 2012, he was a Research Associate with the University of Padova. In 2012, he moved to the Faculty of Science and Technology, Free University of Bozen-Bolzano, Bolzano, Italy, to start research and educational activities in the field of electrical engineering and electrical machines. He is currently an Associate Professor with the Department of Industrial Engineering, University of Padova. His research interests include working on design, analysis, and control of electric machines and drives, with particular interest in renewable energies and more electric vehicles.

Matteo Berto (Student Member, IEEE) was born in Venice, Italy. He received the B.S., M.S., and Ph.d. degrees in electrical engineering from the University of Padova, Padova, Italy, in 2016, 2018, and 2022, respectively.

He is currently a Motor Controls Engineer working for BorgWarner Systems Eng. GmbH, Nuremberg, Germany. His main research interests include position sensing and sensorless control for ac motors.